JIMESE
Journal of Innovation Materials, Energy, and Sustainable Engineering
JIMESE 4(1): 96–117
ISSN 3025-0307

Institute for Advanced Science, Social and Sustainable Future
MORALITY BEFORE KNOWLEDGE

Electrochemical performance of Na_2MnPO_4F/C cathode synthesized through a solid-state method with variation of carbon concentration between citric acid and coconut shell charcoal

Nugraha Ramadhan[1,*]
[1] *Department of Physics, Faculty of Science and Data Analytics, Institut Teknologi Sepuluh Nopember, Surabaya, East Java 60111, Indonesia.*
* Correspondence: nugrahamdhan@gmail.com

Received Date: December 31, 2025 Revised Date: May 17, 2026 Accepted Date: June 3, 2026

ABSTRACT
Background: The increasing demand for sustainable and low-cost energy storage systems has encouraged the development of sodium-ion batteries as an alternative to lithium-ion batteries. However, the low electronic conductivity and slow Na^+ diffusion kinetics of Na_2MnPO_4F remain major limitations for its cathode performance. **Methods:** In this study, Na_2MnPO_4F/C cathode materials were synthesized using a solid-state method with carbon coating derived from citric acid and coconut shell charcoal at concentrations of 0, 3, 5, and 7 wt.%. **Findings:** Structural characterization confirmed the successful formation of the Na_2MnPO_4F phase, where citric acid at 7 wt.% produced the highest phase purity (99.9%), while coconut shell charcoal achieved the highest purity at 3 wt.% (90.066%). SEM-EDX analysis revealed that increasing carbon concentration influenced particle morphology, elemental distribution, and surface porosity, while FTIR analysis confirmed the presence of Mn–O, PO_4, and C–C bonding within the composites. Electrochemical characterization using EIS demonstrated that carbon coating significantly improved charge-transfer behavior, with the 7 wt.% citric acid sample exhibiting the lowest resistance and the best electron transport capability. **Conclusion:** These findings indicate that carbon coating, particularly using citric acid, effectively enhances the structural stability and electrochemical performance of Na_2MnPO_4F cathodes, highlighting its potential for sustainable sodium-ion battery applications. **Novelty/Originality oh this article:** The use of carbon coating derived from citric acid and coconut shell charcoal at concentrations of 0, 3, 5, and 7 wt.% on Na_2MnPO_4F/C cathode materials successfully improved charge-transfer behavior, structural stability, and electron transport capability, particularly in the 7 wt.% citric acid sample which exhibited the lowest resistance and the best electron transport capability.

KEYWORDS: carbon, citric acid, diffusion, electrochemistry, solid-state.

1. Introduction

Rapid population growth and rapid industrial development have led to a substantial increase in global energy demand, particularly for efficient and sustainable energy storage systems (Yang et al., 2010). In recent decades, lithium-ion batteries (LIBs) have emerged as the dominant energy storage technology because of their high energy density and long cycle life. Nevertheless, their extensive utilization has raised several critical concerns, including the limited availability of lithium resources, high production costs, and environmental

Cite This Article:
Ramadhan, N. (2026). Electrochemical performance of Na2MnPO4F/C cathode synthesized through a solid-state method with variation of carbon concentration between citric acid and coconut shell charcoal. *Journal of Innovation Materials, Energy, and Sustainable Engineering, 4*(1), 96-117. https://doi.org/10.61511/jimese.v4i1.2026.2692

issues associated with the extraction of critical elements such as lithium, cobalt, and nickel (Harper et al., 2019; Wu et al., 2018). Furthermore, the continuously increasing global demand for LIBs has intensified pressure on lithium reserves, which are estimated to be only around 20 mg/kg in nature, with nearly 70% concentrated in South America (Zhang, 2017). Such dependence on geographically limited resources is expected to further increase production costs, especially for large-scale energy storage applications such as power grids. Consequently, the development of alternative energy storage technologies that are more sustainable and cost-effective has become increasingly important.

One of the most promising alternatives is sodium-ion batteries (SIBs), which employ sodium as the charge carrier. Sodium is more abundant, more evenly distributed, and more environmentally friendly than lithium (Rojo et al., 2018). In addition, sodium resources are globally accessible and require lower extraction costs, thereby reducing the risk of resource monopolization (Wu et al., 2018). Although the electrochemical performance of SIBs is generally lower than that of LIBs, continuous research efforts have focused on improving their properties through various material design and engineering strategies (Wu et al., 2011; Yao et al., 2024). Among the various approaches, the optimization of cathode materials has attracted significant attention, particularly polyanionic compounds such as phosphates and fluorophosphates, which exhibit excellent structural stability, high thermal safety, and relatively high operating voltages due to the inductive effect of the anionic groups.

In this context, manganese-based fluorophosphate materials have become increasingly attractive because manganese is abundant, inexpensive, and environmentally benign. These characteristics make Mn-based fluorophosphate cathodes a promising pathway toward achieving a balance between energy density, safety, and sustainability (Ahsan et al., 2024; Niu, Zhao, & Xu, 2023; Jin et al., 2020). Among them, Na_2MnPO_4F is considered one of the most promising members of the fluorophosphate family because it theoretically delivers a capacity of approximately 124 mAh g^{-1} through the extraction of one Na^+ ion, with an operating voltage plateau around 3.6 V (Dacek et al., 2016). Such characteristics indicate its strong potential to provide competitive energy density for sodium-ion battery applications.

Despite its promising theoretical properties, the practical application of Na_2MnPO_4F remains limited by its intrinsically low electronic conductivity and sluggish Na^+ diffusion kinetics. These limitations result in poor rate capability and unsatisfactory electrochemical performance. Previous studies have shown that the reversible capacity, cycling stability, and rate performance of Na_2MnPO_4F are highly dependent on particle size, phase purity, and the effectiveness of the conductive network surrounding the active material (Kim et al., 2012). Therefore, improving the electrochemical performance of Na_2MnPO_4F requires not only optimization of the active phase synthesis but also careful microstructural control and conductive interface engineering.

To address these limitations, various modification strategies have been developed, including particle size reduction, ion doping, and surface modification through carbon coating (Wu et al., 2018; Zhang et al., 2025). Among these approaches, carbon coating has been widely recognized as one of the most effective methods for enhancing electronic conductivity, facilitating charge transfer, and improving structural stability during electrochemical processes. Previous studies have demonstrated that carbon-coated Na_2MnPO_4F materials exhibit significantly better electrochemical performance than uncoated materials (Wu et al., 2018). The conductive carbon layer effectively reduces internal resistance and provides more efficient electron transport pathways, leading to improved capacity retention and cycling stability. Furthermore, the incorporation of advanced carbon materials, such as graphene-based structures, has been reported to further enhance conductivity and sodium-ion storage performance (Zhu et al., 2016).

In line with these developments, several strategies have been reported to improve the electrochemical behavior of Na_2MnPO_4F, including the fabrication of carbon composites through spray-drying, carbon-coated micro/nano aggregates, electrospun carbon nanofibers, and dual confinement systems utilizing reduced graphene oxide (rGO) or other carbon nanostructures (Lin et al., 2014; Zhong et al., 2015; Hu et al., 2018). The primary

objective of these strategies is to shorten ion diffusion pathways, reduce charge-transfer resistance, and establish continuous electron transport networks during the sodiation/desodiation process. Compared with other fluorophosphate cathodes that exhibit exceptionally high rate capability, such as carbon-coated $Na_3V_2(PO_4)_2F_3$, Na_2MnPO_4F still offers considerable room for optimization while maintaining the economic advantage of manganese-based composition (Broux et al., 2018; Sui et al., 2021).

The effectiveness of carbon coating is strongly influenced by the type of carbon precursor used. Organic compounds such as citric acid are commonly employed because they can produce relatively uniform carbon layers during thermal decomposition (Huang et al., 2022). However, in recent years, biomass-derived carbon materials have attracted increasing attention as sustainable and low-cost alternatives. Biomass sources such as coconut shell charcoal are abundant, renewable, and environmentally friendly, making them attractive candidates for carbon coating applications in battery materials. In addition to lowering production costs, the utilization of biomass-derived carbon also supports waste valorization and sustainable material development. Coconut shell charcoal, in particular, possesses a high surface area and good electrical conductivity, which can contribute to enhanced electrochemical performance (Siburian, 2019). Moreover, the growing interest in biomass-derived carbon precursors further highlights the relevance of sustainable carbon-coating approaches for polyanionic cathode materials (Sun et al., 2022).

Based on these considerations, this study aims to identify a more cost-effective and accessible carbon source by utilizing coconut shell charcoal as an alternative to citric acid. The use of biomass-derived carbon is also expected to provide environmental benefits while reducing overall production costs (Safitri et al., 2023). In this work, Na_2MnPO_4F/C cathode materials were synthesized using the solid-state method with varying carbon contents of 3 wt.%, 5 wt.%, and 7 wt.% employing both citric acid and coconut shell charcoal as carbon sources. This study specifically investigates the effect of carbon source variation on the structural characteristics and electrochemical performance of the synthesized materials. The findings are expected to contribute to the development of more sustainable, cost-effective, and high-performance cathode materials for sodium-ion battery applications.

2. Methods

The selection of synthesis and carbon-coating approaches for Na_2MnPO_4F materials was based on literature findings indicating that the electrochemical performance of this material is strongly influenced by crystallite size, the homogeneity of carbon distribution, and the continuity of the conductive network surrounding the active particles. In this fluorophosphate system, approaches based on electrospinning, hydrothermal dual-carbon confinement, and carbon-fiber architecture design have been proven effective in producing small-sized particles, improving interfacial contact, and providing more efficient electron/ion transport pathways (Hu et al., 2018; Ling et al., 2019). Therefore, in this study, the synthesis and carbon-coating strategies are positioned not merely as material preparation steps, but as key variables for controlling reaction kinetics and structural stability during the charge–discharge process.

2.1 Research equipment and materials

The main equipment used in this study includes a high-energy ball milling machine equipped with zirconia balls, which was employed to ensure homogeneous mixing and reduce the particle size of the precursor materials. The use of zirconia balls was specifically chosen to minimize contamination during the milling process. A 400-mesh sieve was subsequently utilized to obtain a uniform particle size distribution prior to further processing. For the thermal treatment stage, a vacuum furnace was used during calcination to provide a controlled atmosphere, preventing unwanted oxidation and facilitating the formation of the desired crystal phase.

The primary raw materials for the synthesis of Na_2MnPO_4F/C consist of sodium hydroxide (NaOH) as the sodium source, ammonium dihydrogen phosphate ($NH_4H_2PO_4$) as the phosphate precursor, manganese carbonate ($MnCO_3$) as the manganese source, and sodium fluoride (NaF) as the fluorine source. Citric acid ($C_6H_8O_7$) was incorporated as both a chelating agent and carbon precursor to enhance the uniformity of elemental distribution and to assist in the formation of a conductive carbon coating. Additionally, coconut shell charcoal was used as an external carbon source due to its high carbon content, availability, and environmentally friendly nature, which contributes to improving the electrical conductivity of the final composite material.

2.2 Synthesis of Na_2MnPO_4F

The Na_2MnPO_4F/C composite was synthesized using a solid-state method with sodium hydroxide (NaOH), ammonium dihydrogen phosphate ($NH_4H_2PO_4$), manganese carbonate ($MnCO_3$), and sodium fluoride (NaF) as precursor materials. All precursors were measured based on stoichiometric ratios to obtain the desired phase composition. Carbon sources in the form of citric acid and coconut shell charcoal were added with variations of 0, 3, 5, and 7 wt.% to study their influence on the structural and morphological properties of the material.

Prior to synthesis, the coconut shell charcoal was subjected to a pre-treatment process. The material was first carbonized at 400 °C for 5 hours, followed by chemical activation using KOH to enhance its surface area. The activated carbon was then washed with 1 M HCl solution and rinsed with distilled water until neutral pH was achieved to remove impurities and residual activating agents. The synthesis process was carried out using wet high-energy ball milling with a mass ratio of precursor, zirconia balls, and ethanol of 1 : 5 : 5/3. The mixture was milled for 3 hours to ensure homogeneity, followed by drying at 120 °C for 1 hour. The dried powder was then ground and subjected to thermal treatment. For samples containing citric acid, a pre-carbonization step at 400 °C for 4 hours was performed before calcination at 800 °C for 6 hours. Meanwhile, samples with coconut shell charcoal were directly calcined at 800 °C for 6 hours under an inert atmosphere.

After calcination, the obtained powders were sieved using a 400-mesh sieve to achieve uniform particle size distribution. The synthesized materials were characterized using X-ray Diffraction (XRD) to identify crystalline phases, Fourier Transform Infrared Spectroscopy (FTIR) to analyze functional groups, and Scanning Electron Microscopy coupled with Energy Dispersive X-ray (SEM-EDX) to observe morphology and elemental composition.

2.3 X-Ray diffraction (XRD) analysis

X-Ray diffraction (XRD) analysis was employed to identify the crystalline phases and evaluate the structural properties of the synthesized Na_2MnPO_4F/C cathode materials. The analysis was conducted for samples with carbon content variations of 3 wt.%, 5 wt.%, and 7 wt.% to examine the influence of carbon addition on phase formation and crystallinity. In addition to qualitative phase identification, quantitative analysis was performed to estimate crystallite size and phase composition based on the diffraction patterns.

The XRD measurements were carried out using the Philips X'Pert PRO X-ray diffractometer located at the Materials and Metallurgical Engineering Laboratory, Institut Teknologi Sepuluh Nopember. The diffraction data were collected over a scanning range of 2θ typically between 10° and 80°, using Cu Kα radiation (λ = 1.5406 Å) as the X-ray source. The obtained diffraction patterns were then analyzed and compared with standard reference data to confirm phase purity and identify any secondary phases present in the samples.

Furthermore, the crystallite size of the synthesized materials was estimated using the Scherrer equation based on the full width at half maximum (FWHM) of the diffraction peaks. Phase characterization was carried out using X-ray diffraction (XRD) to confirm the

formation of the target phase and detect the possible presence of impurity phases, while the crystallite size was estimated using the Scherrer equation. The application of this equation is important for comparative studies; however, its interpretation must be conducted carefully because peak broadening is influenced not only by crystallite size, but also by lattice strain, crystal anisotropy, and instrumental contributions (Patterson, 1939; Langford & Wilson, 1978). To complement this information, SEM/TEM observations and EDX compositional mapping were employed to evaluate particle morphology, the degree of agglomeration, the homogeneity of elemental distribution, and the continuity of the carbon coating layer, as commonly recommended in studies on sodium-ion polyanionic cathode characterization (Guo et al., 2023).

2.4 Fourier transform infrared (FTIR) analysis

Fourier Transform Infrared (FTIR) spectroscopy was employed to identify the functional groups present and to analyze the chemical bonding characteristics of the synthesized Na_2MnPO_4F/C cathode materials. This technique is widely used to detect vibrational modes of molecular bonds, allowing for the identification of specific functional groups and confirmation of compound formation. In this study, FTIR analysis was performed to verify the presence of phosphate groups, carbon-related functional groups, and other bonding interactions within the composite material. The analysis also aims to evaluate how the incorporation of carbon sources influences the chemical structure and bonding environment of the material.

The FTIR measurements were carried out at the Chemistry Department Laboratory, Institut Teknologi Sepuluh Nopember, using a standard FTIR spectrometer operating in the mid-infrared region. The spectra were recorded in the wavenumber range of 400–4000 cm^{-1} with sufficient resolution to ensure accurate detection of characteristic absorption peaks. Prior to measurement, the samples were prepared using a conventional method such as KBr pellet or direct measurement technique, depending on the instrument configuration, to obtain high-quality spectra. These preparation steps are essential to minimize noise and ensure reliable spectral interpretation.

The obtained FTIR spectra are presented in the form of transmittance (%) as a function of wavenumber (cm^{-1}), which reflects the absorption behavior of infrared radiation by different functional groups. Characteristic absorption peaks corresponding to PO_4^{3-} groups, C–C bonds, and other relevant functional groups were carefully analyzed to confirm the successful formation of the Na_2MnPO_4F/C structure. In addition, shifts in peak positions and changes in intensity were evaluated to understand the interaction between the active material and the carbon phase. The FTIR results were further correlated with other characterization techniques to provide a comprehensive understanding of the structural and chemical properties of the synthesized materials.

2.5 Scanning electron microscopy-energy dispersive X-ray (SEM-EDX) analysis

Scanning electron microscopy–energy dispersive X-ray (SEM-EDX) analysis was conducted to investigate the surface morphology and elemental distribution of the synthesized Na_2MnPO_4F/C composites. This analysis is particularly important to evaluate the effect of different carbon sources, namely citric acid and coconut shell charcoal, on the microstructure of the material. The SEM observations provide information regarding particle shape, size, and agglomeration behavior, which are closely related to the material's electrochemical performance.

In addition, EDX analysis was employed to determine the elemental composition and to examine the distribution of key elements such as Na, Mn, P, O, F, and C within the composite. The presence and uniform distribution of carbon are essential to enhance electrical conductivity and improve overall material performance. The combined SEM-EDX results allow for a comprehensive understanding of how the synthesis method and carbon

variation influence the structural and compositional characteristics of the Na_2MnPO_4F/C material.

2.6 Electrochemical performance of Na_2MnPO_4F/C cathodes

Electrochemical performance was conducted to evaluate the charge storage behavior and reaction kinetics of the synthesized Na_2MnPO_4F/C cathode materials. This analysis is particularly important to understand the influence of different carbon sources, namely citric acid and coconut shell charcoal, on the electrochemical performance of the material. The presence and uniform distribution of carbon play a crucial role in facilitating electron transport and maintaining structural stability during repeated cycling. Electrochemical characterization was conducted using cyclic voltammetry (CV), Charge–Discharge (CD), and electrochemical impedance spectroscopy (EIS), as these three techniques complement each other in mapping the redox behavior, reversible capacity, polarization, rate capability, and charge-transfer resistance of the material (Zhang et al., 2024). CV was employed to identify redox peak pairs and evaluate the reversibility of the intercalation reactions, while galvanostatic charge–discharge measurements provided direct information regarding specific capacity, coulombic efficiency, cycling stability, and voltage plateau characteristics. Meanwhile, EIS was utilized to examine solution resistance, charge-transfer resistance, and ionic diffusion contributions; however, equivalent-circuit modeling must remain based on physically reasonable models rather than merely producing good numerical fitting results (Gaddam et al., 2021; Kim et al., 2020).

The CV measurements reveal the redox behavior associated with the reversible Mn^{2+}/Mn^{3+} couple during Na^+ intercalation and deintercalation processes, where well-defined oxidation and reduction peaks indicate good electrochemical reversibility. Furthermore, CD result show characteristic voltage plateaus corresponding to these redox reactions, with specific capacity and cycling stability being strongly influenced by the effectiveness of carbon in enhancing electronic conductivity. In addition, EIS analysis is employed to investigate charge transfer resistance and ion diffusion, where a smaller semicircle diameter reflects lower resistance and improved electrochemical kinetics.

3. Results and Discussion

This study uses two variations of the cathode sources, namely citric acid, which is referenced from the study by Safitri et al. (2023), and reduced graphene oxide, with three additional variations of carbon percentages. To facilitate identification, sample codes are given, namely NMPF0 (Na_2MnPO_4F without carbon addition), NMPF3 (with 3% carbon), NMPF5 (with 5% carbon), and NMPF7 (with 7% carbon). Each variation was then tested through several characterization methods to obtain a comprehensive understanding of the crystal structure, morphology, element composition, and functional groups formed. XRD characterization was used to identify the crystalline phases present in each sample, as well as to calculate the relative percentage of the main and secondary phases. SEM analysis was conducted to observe the surface morphology and particle size distribution, providing insight into the homogeneity and potential for agglomeration. EDX was used to determine the elemental composition of the samples, not only to observe the distribution of carbon but also to analyze the percentage of key elements such as Na, Mn, P, O, F, and C. Finally, FTIR was used to analyze the functional groups present in the material, such as the potential contributions from carbon-derived functional groups. Additionally, the transmittance values obtained from the FTIR spectrum were related to the absorption levels, offering insights into the chemical bonding interactions within the material.

3.1 Results of microstructure and morphology characterization tests of Na_2MnPO_4F/C cathode material with carbon concentration variations (Citric Acid)

The phase identification process in the XRD test was carried out qualitatively using the MATCH! software and quantitatively using the HighScore Plus software. The XRD test results using MATCH! are shown in Fig 1.

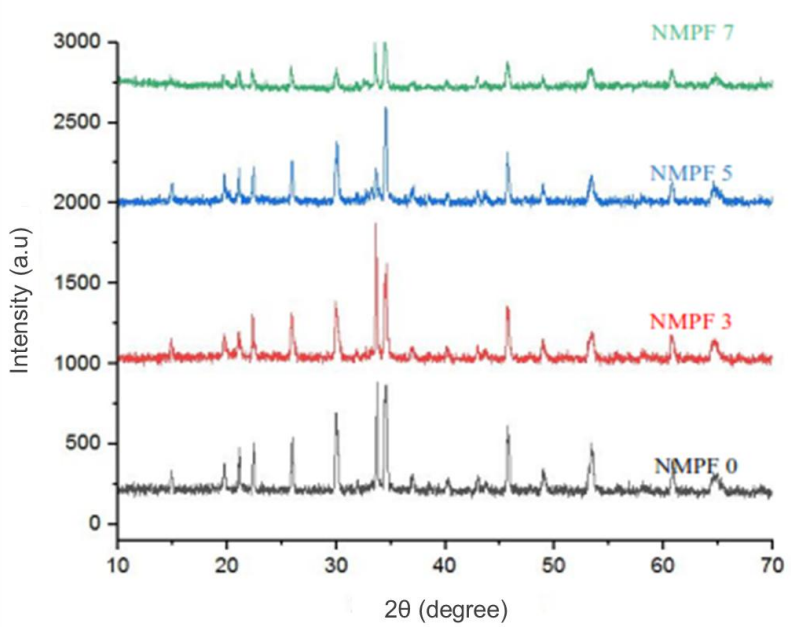

Fig. 1. XRD patterns of Na_2MnPO_4F/C with citric acid–derived carbon at different carbon concentrations

The X-ray diffraction (XRD) analysis results show that the Na_2MnPO_4F phase with a monoclinic structure is formed in all tested samples, both in the sample without carbon (NMPF0) and in the samples with varying carbon concentrations (NMPF3, NMPF5, and NMPF7). The diffraction pattern reveals a main peak in the 2θ range of approximately 20-30°, which is characteristic of the Na_2MnPO_4F phase. The intensity of the main peak is higher in the NMPF 0 sample, indicating that the Na_2MnPO_4F phase is formed with higher purity in the sample without carbon. In contrast, in the samples with added carbon, the intensity of the main peak decreases slightly, and secondary peaks also appear, indicating the possible formation of side phases from the carbon source (citric acid or coconut shell charcoal) used. The addition of carbon plays a role in modifying the material's structure and may influence the electrochemical properties of the material.

Table 1. Phase analysis of Na_2MnPO_4F/C (citric acid–derived carbon) was performed using HighScore Plus software

Sample	Compound	Amount
NMPF0	(Na_2MnPO_4F)	99.4%
	(Na_3PO_4)	0.6%
NMPF3	(Na_2MnPO_4F)	89.9%
	Tetrasodium Diphosphate(V) ($Na_4P_2O_7$)	9.7%
	Manganese Oxide (MnO)	0.4%
NMPF5	(Na_2MnPO_4F)	98.2%
	Trisodium Phosphate(V) (Na_3PO_4)	1.6%
	Manganese Oxide (MnO)	0.2%
NMPF7	(Na_2MnPO_4F)	99.9
	Ramsdellite (Mn_4O_8)	0.1%

A comparison between the NMPF3, NMPF5, and NMPF7 samples shows that as the carbon concentration increases, more side phases are formed, although the Na_2MnPO_4F main phase remains dominant. This suggests that while carbon acts as an additive, it does not significantly interfere with the formation of the main phase. The presence of secondary phases may also indicate the influence of carbon on the crystal structure, which could be related to changes in crystal size or phase distribution, potentially affecting the material's properties such as electrical conductivity and thermal stability. Thus, although all samples contain the main Na_2MnPO_4F phase, varying carbon concentrations can influence the quality and final characteristics of the material produced.

The table presents the phase composition analysis results for various Na_2MnPO_4F samples with different carbon concentrations obtained from the XRD test. Each sample predominantly contains Na_2MnPO_4F as the main phase, but the composition varies depending on the amount of carbon added.

The NMPF0 (no carbon) sample shows that the main phase formed is Na_2MnPO_4F, with a purity of 99.4%. A small amount of Na_3PO_4 (0.6%) is detected as a secondary phase, indicating slight contamination or the formation of a side phase in this sample. The NMPF3 (with 3% carbon) sample still predominantly contains Na_2MnPO_4F at 89.9%, but also shows the formation of secondary phases such as Tetrasodium Diphosphate(V) ($Na_4P_2O_7$) at 9.7%, and Manganese Oxide (MnO) at 0.4%. The addition of carbon in this sample leads to the formation of more secondary phases, which might be due to the influence of carbon or contamination during synthesis. In the NMPF5 (with 5% carbon) sample, Na_2MnPO_4F remains the dominant phase at 98.2%, with secondary phases including Trisodium Phosphate(V) (Na_3PO_4) at 1.6% and Manganese Oxide (MnO) at 0.2%. The carbon addition in this sample slightly increases the contamination with phosphate and manganese oxide phases. Finally, the NMPF7 (with 7% carbon) sample shows nearly complete Na_2MnPO_4F formation with 99.9% purity, with a small trace of Ramsdellite (Mn_4O_8) detected at 0.1%. This suggests that at higher carbon concentrations, manganese oxide phases are less likely to form, although small amounts are still detected.

SEM-EDX characterization of Na_2MnPO_4F/C cathode samples with carbon concentrations of 0, 3, 5, and 7 wt.% was performed to examine the surface morphology, particle distribution, and to investigate the carbon distribution in the samples. The carbon distribution in the samples was analyzed qualitatively and quantitatively. The SEM results for each sample are shown in Fig 2.

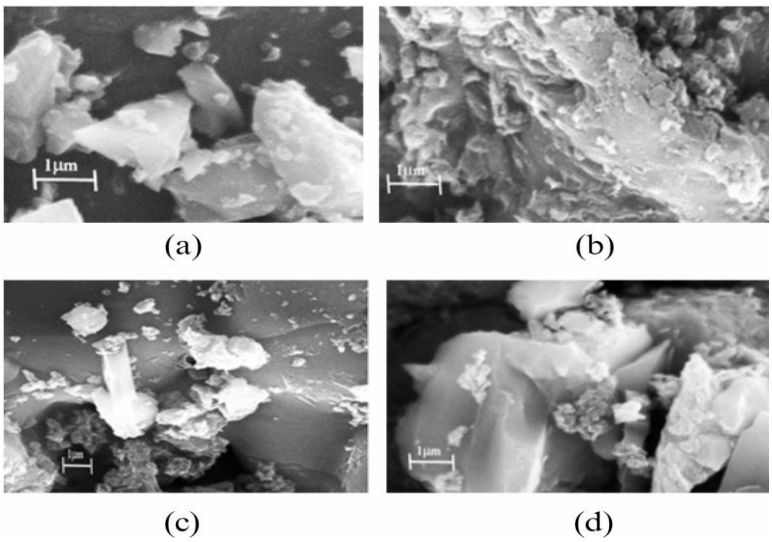

Fig. 2. SEM Characterization of Na_2MnPO_4F/C (citric acid–derived carbon): (a) NMPF0; (b) NMPF3; (c) NMPF5; (d) NMPF7

The SEM-EDX images provide detailed information on the surface morphology and particle distribution of Na_2MnPO_4F/C cathode samples with varying carbon concentrations

of 0, 3, 5, and 7 wt%. In Image (a), representing the sample with no carbon (NMPF0), the particles are larger and more aggregated, showing a smooth and uniform surface. This indicates that without carbon, the particles are relatively crystalline and less disrupted. Image (b), for the 3 wt% carbon sample (NMPF), reveals a rougher surface with smaller, more scattered particles. The addition of carbon at this concentration likely causes the disruption of larger particles, leading to more irregularly shaped grains.

In Image (c), corresponding to the 5 wt% carbon sample (NMPF5), the surface becomes even rougher, with a more heterogeneous particle distribution. This suggests that higher carbon concentrations may lead to the formation of pores or voids within the particles, potentially affecting ion diffusion and conductivity. Image (d), for the 7 wt% carbon sample (NMPF7), shows the most pronounced surface irregularity and porosity, indicating that at this higher concentration, the structure of the particles becomes more disrupted. This may influence the material's stability and electrochemical performance. Overall, as the carbon content increases, the surface morphology becomes increasingly irregular and porous, which could enhance electrochemical performance by increasing the material's surface area and conductivity.

Table 2. Elemental Composition (wt.% or at.%) of Na_2MnPO_4F/C (citric acid–derived carbon)

Sample	O (%)	Mn (%)	Na (%)	P (%)	C (%)
NMPF 0	35.03	26.03	21.32	17.62	0
NMPF 3	35.07	21.2	18.82	17.1	1.8
NMPF 5	35.74	27.24	18.63	16.42	1.97
NMPF 7	35.8	26.48	18.65	16.96	2.11

The table provides the elemental composition of Na_2MnPO_4F/C cathode samples with varying carbon concentrations of 0, 3, 5, and 7 wt%. For NMPF0 (no carbon), the sample contains 35.03% oxygen, 26.03% manganese, 21.32% sodium, and 17.62% phosphorus, with no detectable carbon (0%). This composition represents a typical stoichiometric Na_2MnPO_4F structure, where the balance of elements is as expected without the influence of carbon. In NMPF3 (with 3% carbon), the oxygen content increases slightly to 35.07%, while the manganese content decreases to 21.2% and sodium to 18.82%. Phosphorus is at 17.1%, with carbon detected at 1.8%. The addition of carbon results in a reduction in the manganese and sodium percentages, suggesting that the presence of carbon affects the overall elemental distribution within the material, potentially altering the phase formation or particle morphology.

For NMPF5 (with 5% carbon), the oxygen content rises further to 35.74%, and manganese increases to 27.24%, indicating that higher carbon concentrations may promote a greater incorporation of manganese. However, the sodium content decreases to 18.63%, and phosphorus to 16.42%. The carbon content increases to 1.97%, continuing to influence the elemental distribution. This suggests that the addition of carbon not only impacts the structural properties but also slightly shifts the proportions of other elements. Finally, in NMPF7 (with 7% carbon), the oxygen content is 35.8%, and manganese is slightly reduced to 26.48%, while sodium is at 18.65% and phosphorus at 16.96%. The carbon content reaches 2.11%, showing a further increase in carbon concentration, which continues to impact the elemental balance by slightly lowering the sodium and phosphorus content. Manganese remains relatively stable, indicating that the material may maintain its structural integrity despite the increased carbon content.

Overall, as the carbon concentration increases, there are noticeable shifts in the elemental composition, particularly in the reduction of sodium and phosphorus, while oxygen and manganese contents remain relatively stable. This alteration in composition likely reflects the role of carbon in modifying the structure and properties of the Na_2MnPO_4F phase, which could influence the material's electrochemical behavior and performance.

The FTIR characterization results are shown in Figure 3, with the characteristic spectrum of Na_2MnPO_4F displaying several important absorption peaks, and the types of bond wavelengths can be seen in figure 3 and Table 3.

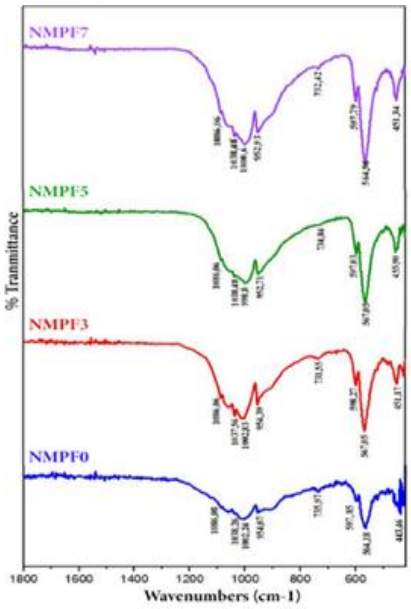

Fig. 3. FTIR Spectra of Na_2MnPO_4F/C Cathode Samples (citric acid–derived carbon) with 0, 3, 5, and 7 wt.% carbon

The FTIR (fourier transform infrared) analysis results shown in Figure 3 provide valuable insights into the vibrational modes of the samples with varying carbon concentrations (NMPF0, NMPF3, NMPF5, and NMPF7). In NMPF0 (no carbon), the FTIR spectrum reveals a distinct C-C bond at around 1120 cm^{-1}, which can be attributed to the carbon source derived from the decomposition of NaOH and $MnCO_3$ during the synthesis process. This peak suggests that even without intentional carbon addition, some residual carbon remains within the sample due to the decomposition of precursors.

As the carbon content increases in NMPF3, NMPF5, and NMPF7, the FTIR spectra show additional characteristic peaks corresponding to C-C stretching vibrations, particularly around 1,000 cm^{-1} and 1,400 cm^{-1}. These peaks are attributed to the C-C bonds originating from the decomposition of citric acid, which was used as a carbon source in these samples. The appearance of these peaks indicates that the added carbon is effectively incorporated into the structure, and the carbon from citric acid is now an integral part of the material. In NMPF3, the intensity of the C-C bonds is relatively lower compared to NMPF5 and NMPF7, which suggests that a higher concentration of carbon leads to more significant incorporation into the Na_2MnPO_4F matrix. This trend is reflected in the increase in peak intensities as the carbon content rises, with NMPF7 showing the most prominent C-C stretching vibrations, indicating the highest degree of carbon incorporation.

Table 3. Bond assignments and corresponding wavenumbers of Na_2MnPO_4F/C (citric acid–derived carbon)

Type of Bond	Wavenumber (cm^{-1})				
	Range	NMPF0	NMPF3	NMPF5	NMPF7
Mn-O	451- 597	443.4	451.2	455.9	451.54
		564.2	567.1	565.2	564.96
		597.6	598.3	597.03	597.8
		954.1	954.4	952.7	951.9
PO_4	955- 1,000	1,002.2	1,002.4	998.8	1,000.6
		1,038.3	1,037.6	1,038.5	1,038.5
C-C	800- 1,011	1,086.1	1,086.1	1,086.7	1,086.1

The FTIR data table presents characteristic bonds in Na_2MnPO_4F/C samples with varying carbon concentrations (NMPF0, NMPF3, NMPF5, and NMPF7) in specific wavenumber ranges. The Mn-O bond, related to the Mn-O vibrations in the Na_2MnPO_4F

structure, is detected at several peaks between 451 cm^{-1} and 597 cm^{-1}. In NMPF 0, the Mn-O peaks appear at 443.4 cm^{-1}, 564.2 cm^{-1}, and 597.6 cm^{-1}, with an additional peak at 954.1 cm^{-1}. When carbon is added in NMPF3, NMPF5, and NMPF7, these Mn-O peaks remain in the same range, although slight shifts in the peaks and variations in intensity are observed. This indicates that the Mn-O bond remains stable even with the incorporation of carbon into the structure.

For the PO_4 bond, associated with P-O vibrations in the phosphate group, the main peaks are detected around 1,000 cm^{-1} and 1,038 cm^{-1}. In NMPF 0, the PO_4 peaks appear at 1,002.2 cm^{-1} and 1,038.3 cm^{-1}, while in NMPF3, NMPF5, and NMPF7, the positions of the PO_4 peaks shift slightly, but they remain within the characteristic range, indicating that the phosphate structure is preserved despite the carbon addition.

Finally, the C-C bond is detected in the 800-1,011 cm^{-1} range, indicating the presence of carbon incorporated into the structure. In all samples (NMPF0, NMPF3, NMPF5, and NMPF7), the C-C peak is detected around 1086 cm^{-1}, suggesting that the carbon-C bond remains present, even though carbon was introduced in the form of citric acid in the higher carbon concentration samples. This indicates that the carbon integrated into the structure remains stable.

3.2 Results of microstructure and morphology characterization tests of Na_2MnPO_4F/C cathode material with carbon concentration variations (reduced graphene oxide)

Phase identification in the XRD analysis was carried out qualitatively using OriginPro 2023b and quantitatively using QualX, with the results shown in Fig 4.

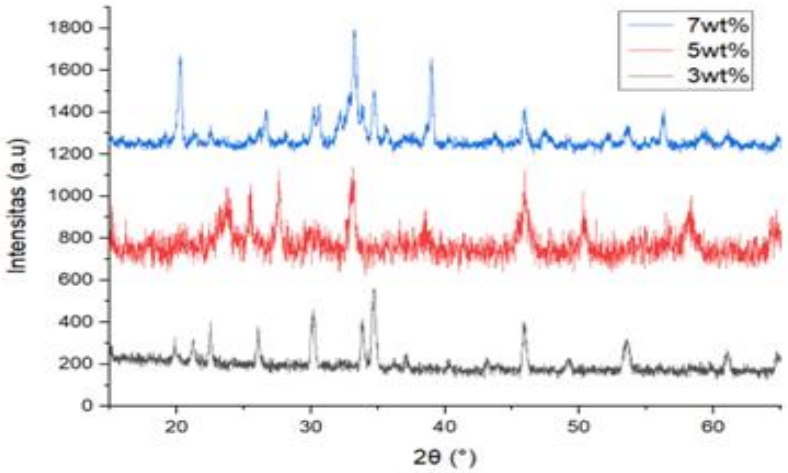

Fig. 4. XRD Patterns of Na_2MnPO_4F/C with different carbon concentrations (reduced graphene oxide, rGO)

Phase identification was performed using QualX, as summarized in Table 4. In practice, the analysis starts from the experimental XRD patterns that the background is corrected, the main reflections are picked, and the resulting peak positions are then matched against reference patterns in the database (search–match). After the most plausible candidates are selected, QualX estimates the phase contribution by checking how well the reference peaks align with the experimental peaks and how closely the relative intensities can be reproduced over the full 2θ range. This means the evaluation is not limited to "does the target phase appear," but also to whether extra reflections are present, which would signal secondary phases or incomplete reaction.

Phase identification using QualX (Table 4) shows a clear dependence of crystalline composition on carbon content. The NMPF 3 sample contains the highest fraction of the target cathode phase Na_2MnPO_4F, reaching 90.066%, while the remaining fraction is distributed among minor components labeled as Na (2.730%), F_2 (4.112%), and Na_3P (3.092%). These minor assignments should be interpreted cautiously: in search–match

routines, small unmatched reflections can sometimes be represented by simplified database entries. Practically, their presence indicates that NMPF3 is largely dominated by the intended Na_2MnPO_4F framework with only a small amount of secondary contributions, meaning the synthesis route at 3 wt% carbon most effectively favors formation of the desired phase.

Table 4. Phase analysis of Na_2MnPO_4F/C samples with reduced graphene oxide (rGO) carbon variation was carried out using QualX software.

Sample	Compound	Amount
NMPF 3	(Na_2MnPO_4F)	90.066%
	Sodium (Na)	2.730%
	F_2	4.112%
	(Na_3P)	3.092%
NMPF 5	(Na_2MnPO_4F)	57.116%
	P	42.884%
NMPF 7	$Na_4(P_2O_7)$	70.322%
	(Na_2MnPO_4F)	29.678%

When the carbon content is increased, the phase purity decreases significantly. For NMPF5, the Na_2MnPO_4F fraction drops to 57.116%, accompanied by a large non-target contribution assigned as P (42.884%). Regardless of whether this "P" label represents a truly elemental phase or a phosphorus-rich by-product that matches a similar peak set, the result strongly suggests a phosphorus-dominant secondary contribution and indicates that the solid-state reaction is less complete or less selective toward Na_2MnPO_4F under the 5 wt% carbon condition. The trend becomes even more pronounced in NMPF 7, where QualX identifies $Na_4(P_2O_7)$ as the dominant phase (70.322%) and the target Na_2MnPO_4F decreases to 29.678%. The emergence of a pyrophosphate-rich phase implies that at higher carbon loading, phosphate-related side reactions (or structural rearrangements favoring P_2O_7 units) become strongly competitive, diverting the system away from crystallizing Na_2MnPO_4F.

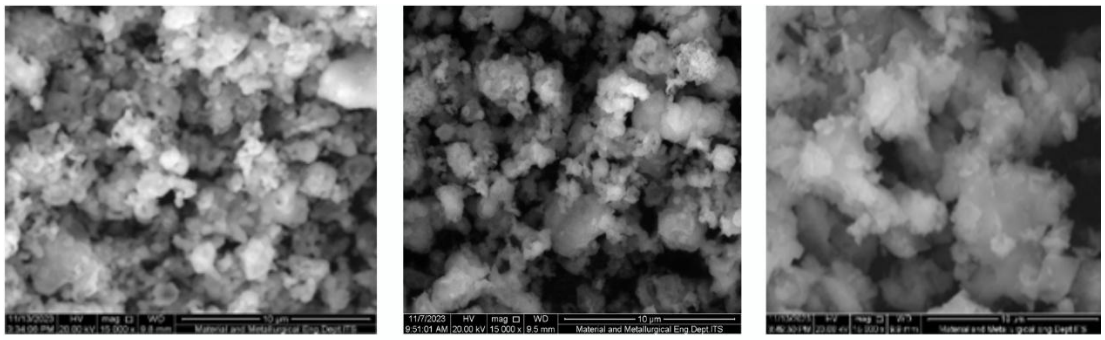

Fig. 5. EDX Characterization of Na_2MnPO_4F/C Cathode Samples (reduced graphene oxide): (a) NMPF3; (b) NMPF5; (c) NMPF7

The carbon distribution was further evaluated by SEM–EDX for Na_2MnPO_4F/C cathodes with 3, 5, and 7 wt% carbon, analyzed both qualitatively (SEM morphology in Figure 5) and quantitatively (EDX composition in Table 5). The SEM images (Fig. 5a–c) show that all samples consist of agglomerated particles, which is typical for solid-state–derived polyanion cathodes. NMPF3 (a) appears as relatively compact clusters of irregular grains. NMPF5, (b) still shows granular agglomerates, but the contrast looks more heterogeneous—often a sign that the surface is starting to be partially covered by a secondary phase or carbon-rich regions. In NMPF7, and (c) the features look more "merged"/coarse and less sharply resolved, which is commonly observed when a sample has stronger surface coverage (e.g., thicker carbon coating or carbon-rich agglomerates)

and/or when the dominant crystalline phase changes, producing a different texture and packing.

Table 5. Elemental composition (wt.% or at.%) of Na_2MnPO_4F/C (reduced graphene oxide, rGO)

Sample	Mn (%)	O (%)	Na (%)	P (%)	F (%)	C (%)
NMPF3	29.13	23.13	22.97	14.91	7.91	1.96
NMPF5	26.65	24.30	21.42	13.79	08.31	05.53
NMPF7	09.94	28.75	26.67	17.46	05.55	11.64

The EDX results (Table 5) support a strong compositional shift with increasing carbon. The carbon signal increases sharply from 1.96% (NMPF3) → 5.53% (NMPF5) → 11.64% (NMPF7). This is more than just a linear increase and strongly suggests that, at higher nominal carbon loading, carbon is not only present but becomes surface-enriched in the analyzed area. That can happen if carbon forms thicker coatings or local carbon clusters, because EDX is surface/near-surface sensitive (and the measured spot may "see" carbon more than the bulk). In parallel, the Mn percentage drops dramatically, especially for NMPF7: 29.13% (NMPF3) → 26.65% (NMPF5) → 9.94% (NMPF7). This large decrease is consistent with two effects happening together: (i) dilution/attenuation of the Mn signal by carbon-rich surface layers, and (ii) a real phase/composition change where Mn-containing Na_2MnPO_4F becomes a smaller fraction of the material. If your XRD/QualX already indicated that NMPF7 is dominated by a Mn-free phosphate/pyrophosphate phase (e.g., $Na_4(P_2O_7)$), the EDX trend (very low Mn but high Na–P–O) matches that picture well.

Looking at the phosphate-related elements, P and O become relatively more prominent in NMPF7 (P = 17.46%, O = 28.75%) compared with NMPF3 (P = 14.91%, O = 23.13%). At the same time, Na increases to 26.67% in NMPF7. This Na–P–O enrichment aligns with the idea that higher-carbon conditions are associated with a stronger contribution from sodium phosphate/pyrophosphate-type chemistry, which reduces the relative fraction of Na_2MnPO_4F. The F content shows a different behavior: it is 7.91% (NMPF3), slightly higher at 8.31% (NMPF5), then drops to 5.55% (NMPF7). A decrease in F at high carbon can indicate that the fluorinated framework is no longer dominant (less Na_2MnPO_4F present), and/or partial F loss/redistribution during synthesis—either way, it again supports that NMPF7 deviates the most from the intended fluorophosphate composition.

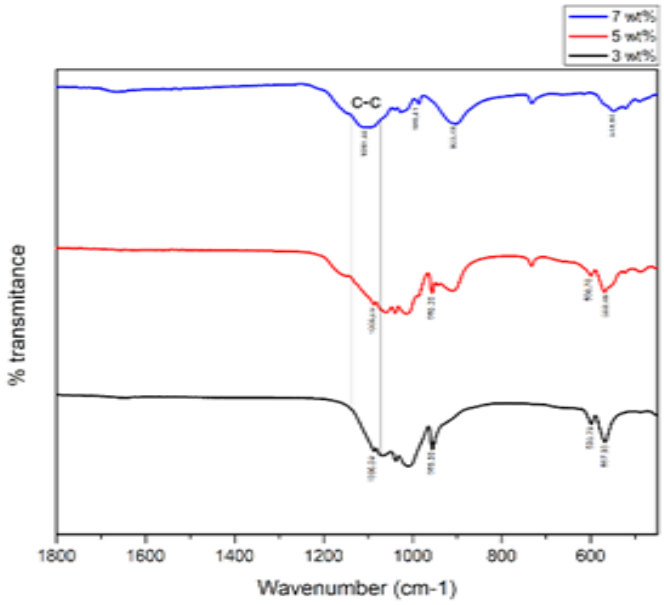

Fig. 6. FTIR spectra of Na_2MnPO_4F/C cathode samples with 3, 5, and 7 wt.% carbon (reduced graphene oxide, rGO)

The FTIR spectra of NMPF3, NMPF5, and NMPF7 (Fig. 6) confirm the presence of the characteristic vibrational features of a phosphate-based polyanion framework, with the

dominant bands arising from PO_4^{3-} units and additional contributions from Mn–O vibrations in the Na_2MnPO_4F/C lattice. In general, the region below ~600 cm^{-1} is commonly associated with metal–oxygen vibrations and bending modes, while the fingerprint region between ~900 and 1050 cm^{-1} is highly sensitive to P–O stretching in tetrahedral phosphate groups. Importantly, the comparison across carbon loadings (3, 5, and 7 wt%) shows systematic peak shifts and band re-organization, indicating changes in the local bonding environment and, potentially, the increasing influence of non-target phosphate-derived phases.

Table 6. Bond assignments and corresponding wavenumbers of Na_2MnPO_4F/C (reduced graphene oxide, rGO)

Type of Bond	Wavenumber (cm^{-1})			
	Range	NMPF3	NMPF5	NMPF7
Mn-O	451- 597	453.12	489.74	491.22
		567.77	568.57	521.84
		598.80	599.26	548.81
PO_4	955- 1,000	955.63	910.77	903.40
		1,010.71	956.35	986.57
		1,037.71	1,012.22	1,027.51
C-C	800- 1,011	1,065.43	1,058.55	1,096.56

In the Mn–O region (451–597 cm^{-1}), NMPF3 exhibits bands at 453.12, 567.77, and 598.80 cm^{-1}, suggesting a relatively well-defined Mn–O environment consistent with the formation of the targeted fluorophosphate framework. With increasing carbon content, these bands shift and partially reorganize. NMPF5 shows bands at 489.74, 568.57, and 599.26 cm^{-1}, where the lowest-frequency Mn–O feature moves from ~453 to ~490 cm^{-1}. Such a shift typically reflects a change in bond stiffness and/or local coordination around Mn, which can arise from subtle lattice distortion, microstructural differences, or the presence of additional phases. The effect becomes more pronounced in NMPF7, where the Mn–O-related features appear at 491.22, 521.84, and 548.81 cm^{-1} and the ~599 cm^{-1} band is no longer observed. The disappearance of the high-wavenumber Mn–O component and the emergence of new bands around ~522 and ~549 cm^{-1} point to a more heterogeneous Mn–O environment and are consistent with a reduced contribution of Mn-containing Na_2MnPO_4F in the 7 wt% carbon sample.

The most diagnostic changes occur in the phosphate region (955–1,000 cm^{-1}). NMPF3 shows a clear phosphate signature with peaks at 955.63 cm^{-1}, accompanied by higher-wavenumber bands at 1,010.71 and 1,037.71 cm^{-1}. These are typically assigned to P–O stretching modes (with contributions from symmetric and asymmetric stretching components of PO_4 tetrahedra). In contrast, NMPF5 and NMPF7 display a strong downshift of the lower phosphate band to 910.77 cm^{-1} and 903.40 cm^{-1}, respectively, followed by bands at 956.35 and 1,012.22 cm^{-1} for NMPF5 and 986.57 and 1,027.51 cm^{-1} for NMPF7. A shift from ~955 cm^{-1} toward ~903–911 cm^{-1} generally indicates a meaningful change in the phosphate bonding environment—such as stronger distortion of PO_4 units, different Na–O–P local arrangements, and/or the growing contribution of phosphate/pyrophosphate-type species with distinct vibrational fingerprints. This interpretation aligns well with the phase evolution observed in XRD/QualX, where higher carbon loadings correlate with a reduced Na_2MnPO_4F fraction and a stronger presence of phosphate-derived secondary phases (particularly for NMPF7).

The C–C-related band (800–1,011 cm^{-1}) is also detected in all samples, appearing at 1,065.43 cm^{-1} (NMPF3), 1,058.55 cm^{-1} (NMPF5), and 1,096.56 cm^{-1} (NMPF7). While FTIR is not the most sensitive technique for detailed carbon structure (Raman would better resolve D/G bands), the persistence of this feature supports the presence of carbon in the composite and its increasing influence on the overall spectral profile. The upward shift to ~1,097 cm^{-1} in NMPF7 may be associated with differences in carbon bonding configuration and/or band overlap with the changing phosphate modes.

3.3 Comparison of characterization results of Na_2MnPO_4F with citric acid and reduced graphene oxide coatings

The synthesis of Na_2MnPO_4F material with two different coatings, citric acid and reduced graphene oxide or coconut shell charcoal, shows distinct characteristics in crystal structure, morphology, elemental composition, and functional groups.

Based on the XRD results, both coatings produced the main phase of Na_2MnPO_4F with diffraction peaks in the 2θ range of 17–35°, in accordance with the JCPDS standard No. 74-2286. However, differences were observed in phase stability. For citric acid coating, the main phase was formed with high consistency, especially in the NMPF7 variation, which reached 99.9%, with only a small amount of the minor Ramsdellite phase (0.1%). This indicates that citric acid is effective as a complexing agent, maintaining the homogeneity of metal ions during the synthesis. In contrast, with rGO coating, the highest pure phase was found in NMPF3 (90.07%), but it drastically decreased in NMPF5 (57.12%) and NMPF7 (29.68%) due to the formation of $Na_4(P_2O_7)$ impurities up to 70.32%. Thus, citric acid provides more consistent phase stability, while rGO is potentially optimal only at certain concentrations.

Morphological analysis through SEM-EDX also showed significant differences. The citric acid sample exhibited a more uniform particle distribution, smoother surfaces, and a thin, homogeneous amorphous carbon layer resulting from citric acid decomposition. On the other hand, rGO particles were relatively homogeneous in NMPF3 but became rough in NMPF5 and showed large agglomeration in NMPF7 due to excess carbon. Elemental composition from EDX confirmed these findings: for citric acid, the main elements (Na, Mn, P, O) were detected, except for F (a light element) due to weak signal intensity that was easily overshadowed by peaks from other elements with higher characteristic energies, along with a thin carbon content (~3.4 at.%) enhancing the conductive layer. For rGO, the carbon content increased significantly (1.96% → 5.53% → 11.64%), which, on one hand, improved conductivity but, at higher concentrations, covered the active surface and interfered with Na^+ ion diffusion.

FTIR analysis revealed that both coatings maintained the characteristic absorption bands of Na_2MnPO_4F, namely the Mn–O vibration at 453–599 cm^{-1} and the PO_4^{3-} stretching at 955–1,038 cm^{-1}. However, differences appeared in the carbon bands. For citric acid, weak C=C (~1,384 cm^{-1}) and –OH (~3,435 cm^{-1}) bands indicated citric acid residues from the main elemental compounds. In contrast, rGO showed C–C (1,065–1,096 cm^{-1}) and C=C (~1,580 cm^{-1}) bands, signifying the presence of graphene. FTIR transmittance data also showed differing trends: for citric acid, transmittance consistently decreased with increased carbon (96.63% → 77.22%), meaning that absorbance increased steadily. For rGO, the transmittance values were more fluctuating (51.37% → 45.78% → 58.82%), indicating that the carbon layer was less stable at higher variations.

Overall, citric acid coating outperforms in terms of phase stability, morphological uniformity, and the formation of a thin, homogeneous carbon layer that supports structural stability and conductivity, especially at the 7 wt.% variation. This aligns with the report by Chen et al. (2019) in the Journal of Power Sources that citric acid acts as an effective complexing agent in maintaining metal ion homogeneity during synthesis, while also forming conductive amorphous carbon layers (Chen et al., 2019). rGO coating offers advantages in enhancing electronic conductivity and can generate a higher pure phase at optimal conditions (NMPF3), but it risks forming impurity phases and agglomeration at excessive concentrations, as reported by Fang et al. (2016) in the Journal of Materials Chemistry A. Therefore, it can be concluded that citric acid provides the best results for structural stability and particle homogeneity, while rGO only delivers optimal performance at low concentrations, particularly at the 3 wt.% variation.

3.4 Results of electrochemical performance testing of Na_2MnPO_4F/C batteries with varying carbon (citric acid) concentrations

3.4.1 Analysis of electrochemical impedance spectroscopy (EIS)

The EIS test results for the Na_2MnPO_4F/C material with varying concentrations of citric acid as the carbon source, namely 0 wt.% (NMPF0), 3 wt.% (NMPF3), 5 wt.% (NMPF5), and 7 wt.% (NMPF7), are shown in Fig 7.

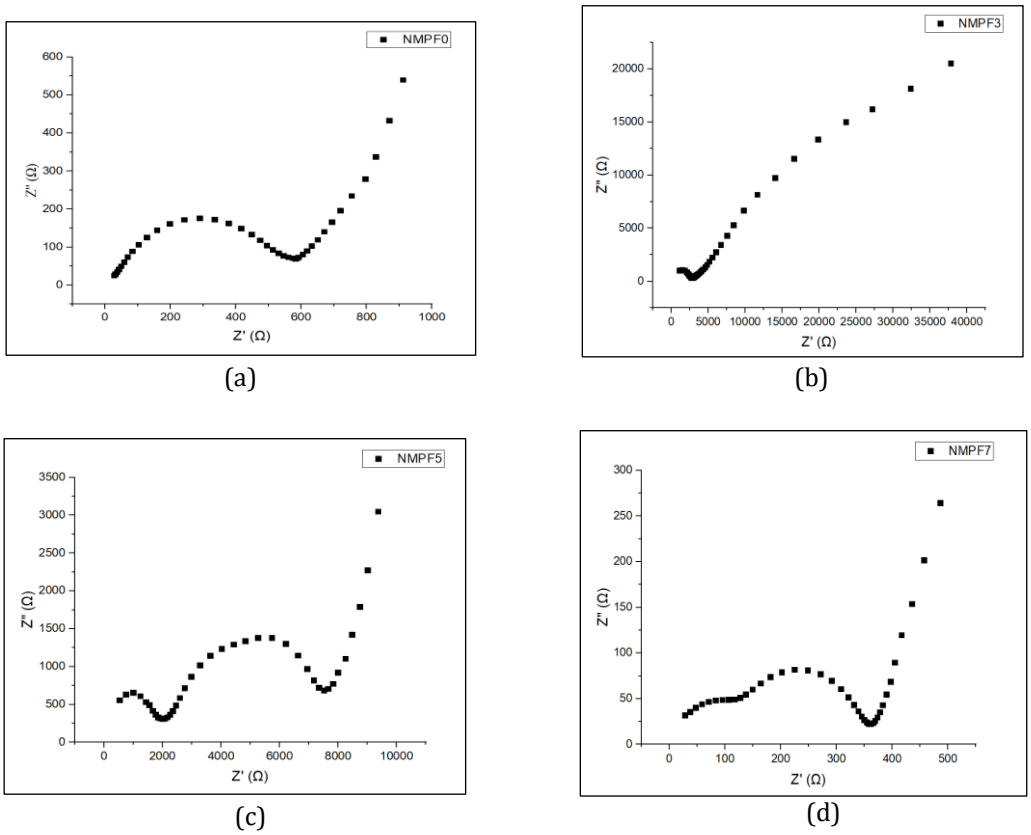

Fig. 7. EIS Test Results for Na_2MnPO_4F/C Cathode Samples with Carbon Variations: (a) NMPF0, (b) NMPF3, (c) NMPF5, and (d) NMPF7

The Nyquist plot in Figure 7 generally consists of two main parts: a semicircle in the high-to-mid-frequency range representing charge transfer resistance (Rct), and a sloping line in the low-frequency range indicating Na^+ ion diffusion (Warburg impedance).

Regarding the semicircle diameter parameter, it can be observed that the sample with a carbon concentration of 7 wt.% has the smallest diameter, indicating the highest electron transfer capability with the lowest resistance. For the semicircle height parameter, it is noted that the NMPF7 sample has the lowest semicircle peak, indicating that the NMPF7 sample possesses the best capacitive properties, effectively reduces the charge transfer barrier, thereby accelerating the kinetics of the electrochemical reaction. For the final parameter, the slope, a high slope indicates a faster ion diffusion process, with the NMPF7 sample exhibiting the steepest slope compared to the other samples.

Analysis of the Nyquist plot correlated with the EIS parameters in Table 7 shows that an increase in carbon content significantly improves the electrochemical properties of the Na_2MnPO_4F/C material. The NMPF7 sample (7 wt.% carbon) exhibited the best performance, with the lowest resistance, highest conductivity, and fastest ion diffusion, making it the optimal composition for sodium-ion battery cathode applications.

Table 7. Electrical and ionic conductivity values and Na+ Ion diffusion coefficients in the battery (Na_2MnPO_4F/C Cathode)

Sample	Re (Ω)	Rct (Ω)	σe (S cm^{-1})	σi (S cm^{-1})	D_{Na+} (cm^2s^{-1})
NMPF0	28,62	588,97	$1,50 \times 10^{-8}$	$3,06 \times 10^{-7}$	$1,95 \times 10^{-16}$
NMPF3	1156,24	2901,88	$0,30 \times 10^{-8}$	$0,07 \times 10^{-7}$	$1,08 \times 10^{-21}$
NMPF5	547,60	2023,77	$0,44 \times 10^{-8}$	$0,16 \times 10^{-7}$	$3,37 \times 10^{-20}$
NMPF7	28,82	362,18	$6,90 \times 10^{-8}$	$3,08 \times 10^{-7}$	$5,51 \times 10^{-16}$

3.4.2 Analysis of cyclic voltammetry (CV)

The potential range used in this CV test was 1.5–4.5 V, with a scan rate of 0.1 mV/s. to evaluate the redox behavior and the reversibility of the electrochemical reaction of the Na_2MnPO_4F/C cathode material with varying carbon content.

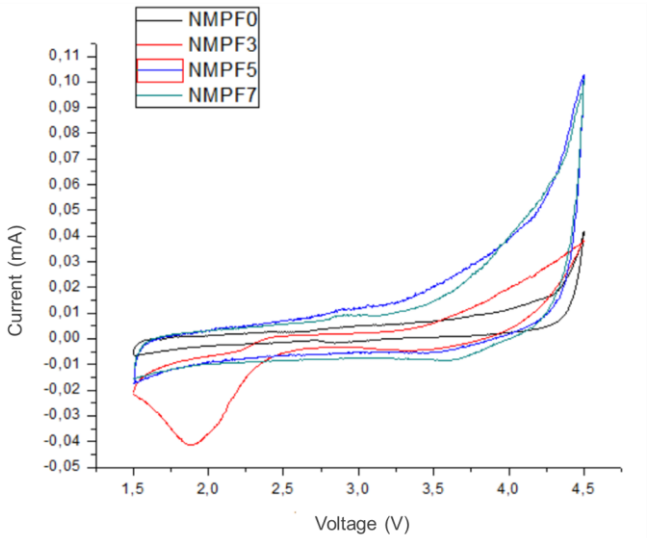

Fig. 8. Cyclic Voltammetry curves for Na_2MnPO_4F/C cathode samples at 0, 3, 5, and 7 wt.%

As shown in Fig 8, all samples exhibit pairs of oxidation and reduction peaks, indicating the occurrence of reversible redox reactions. The oxidation peaks are associated with the release of Na^+ ions (deintercalation), while the reduction peaks indicate the reinsertion of Na^+ ions (intercalation) into the material structure. However, the shape of the curve and the position of the peaks show significant differences among the carbon variants, indicating an influence on reaction kinetics and electrochemical polarization. An important parameter in CV analysis is the voltage difference between the oxidation and reduction peaks (ΔV), which reflects the degree of polarization and the reversibility of the system.

Table 8. Cyclic voltammetry results for a battery (Na_2MnPO_4F/C Cathode) at a scan rate of 0.1 mV/s

Sample	Oxidation Peak		Reduction Peak		ΔV
	Voltage (V)	Current (mA)	Voltage (V)	Current (mA)	
NMPF0	3.03	0.005	4.07	-0.003	1.04
NMPF3	2.50	0.001	1.91	-0.041	0.59
NMPF5	3.07	0.013	3.53	-0.005	0.46
NMPF7	3.09	0.009	3.54	-0.008	0.45

The improved performance of samples with higher carbon content can be explained by the formation of a conductive carbon layer on the particle surface an increase in electron pathways a reduction in charge transfer resistance and polarization. However, at low concentrations (3 wt.%), the carbon is not yet optimally distributed and thus cannot form an effective conductive network.

Based on the CV curve analysis and the data in Table 8, it can be concluded that the addition of carbon has a significant effect on the electrochemical properties of the Na_2MnPO_4F/C material. The NMPF7 sample exhibited the best performance with the smallest ΔV value, relatively high redox current, and good reversibility. This indicates that this composition is capable of improving reaction kinetics and charge transfer efficiency in sodium-ion battery systems.

3.4.3 Analysis of charge-discharge (CD)

In this CD test, the battery samples were subjected to a voltage range of 1.5–4.5 V with a scan rate of 0.1 mV/s. The charge-discharge (CD) test results for the Na_2MnPO_4F/C cathode material are shown in Fig 9.

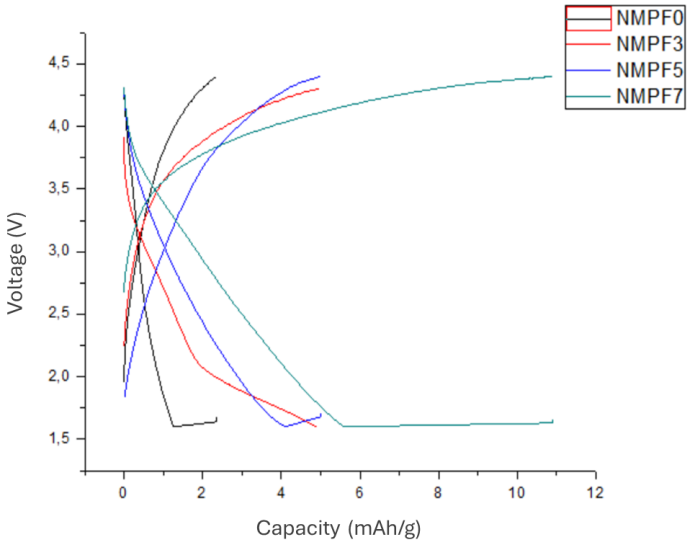

Fig. 9. Charge/discharge curves for Na_2MnPO_4F/C cathode samples at 0, 3, 5, and 7 wt. %

The data in Table 9 show that the charge capacity values for each sample are nearly identical to their discharge capacities, indicating that these samples exhibit good reversibility.

Table 9. Battery capacity results (Na_2MnPO_4F/C cathode)

Sample	Capacity (mAh/g)		Working Voltage (V)
	Discharge	Charge	
NMPF0	2.36	2.36	3.04
NMPF3	4.89	4.98	3.10
NMPF5	5.00	4.99	3.10
NMPF7	10.9	10.9	3.46

In addition, a voltage plateau was observed within a certain range, which is associated with the Mn redox reaction in the Na_2MnPO_4F structure. A more stable and prolonged plateau indicates the stability of the electrochemical reaction throughout the process. The nearly identical charge and discharge capacities across all samples indicate that the coulombic efficiency approaches 100%, meaning energy loss during cycling is very small the electrochemical reaction proceeds reversibly. This is consistent with previous CV results showing that Sample NMPF7 (7 wt.% carbon) exhibits the best performance with the highest specific capacity, Coulombic efficiency approaching 100%, and a higher operating voltage.

4. Conclusions

The variation in carbon concentration (3%, 5%, and 7 wt%) affects the crystal structure, morphology, and elemental composition of the cathode material synthesized using the solid-state method. Characterization results show that using citric acid as the carbon source results in a highly stable Na_2MnPO_4F phase, particularly at the 7 wt% variation, which achieves a purity of 99.9%. In contrast, the use of coconut shell charcoal leads to the formation of more significant side phases, especially at the 7 wt% variation, indicating a decrease in Na_2MnPO_4F purity.

In terms of morphology, the addition of carbon causes an increase in surface irregularity and porosity of the material, which can enhance the surface area and conductivity, thereby improving electrochemical performance. Overall, citric acid is more effective in maintaining phase stability and producing a more homogeneous carbon layer compared to coconut shell charcoal. This research contributes significantly to the development of sodium battery technology with more cost-effective and environmentally friendly materials, supporting the achievement of the Sustainable Development Goals, particularly in providing affordable and clean energy.

Acknowledgement

The authors would like to express their sincere gratitude to Mochamad Zainuri, Dr., Drs., M.Si., for his valuable guidance and supervision throughout the course of this research. The authors also acknowledge the Ministry of Education, Culture, Research, and Technology (Kemendikbudristek) of the Republic of Indonesia for funding this work. Special thanks are extended to the National Achievement Center (Puspresnas) and the Indonesian Talent Development Center (BPTI). Finally, the authors are grateful to Institut Teknologi Sepuluh Nopember for providing institutional support and research facilities.

Author Contribution

The author contributed to all aspects of the study, including conception and design, analysis, and presentation of results.

Funding

This research was funded by the Ministry of Education, Culture, Research, and Technology of the Republic of Indonesia (Kemendikbudristek) through the 2023 Student Creativity Program (PKM).

Ethical Review Board Statement

Not applicable. This study did not involve humans, animals, or issues concerning public health and safety.

Informed Consent Statement

Not applicable. This study did not involve humans.

Data Availability Statement

The data that support the findings of this study are available from the corresponding author upon reasonable request.

Conflicts of Interest

The authors declare no conflict of interest. The funder had no role in the design of the study; in the collection, analyses, or interpretation of data; in the writing of the manuscript; or in the decision to publish the results.

Declaration of Generative AI Use

During the preparation of this work, the authors used ChatGPT (OpenAI) to assist in

improving the English language and refining the structure of the manuscript. After using this tool, the authors reviewed and edited the content as needed and take full responsibility for the content of the publication.

Open Access

References

Ahsan, Z., Cai, Z., Wang, S., Moin, M., Wang, H., Liu, D., Ma, Y., Song, G., & Wen, C. (2024). Recent development of phosphate based polyanion cathode materials for sodium-ion batteries. *Advanced Energy Materials*. https://doi.org/10.1002/aenm.202400373

Broux, T., Fauth, F., Hall, N., Chatillon, Y., Bianchini, M., Bamine, T., Leriche, J.-B., Suard, E., Carlier, D., Reynier, Y., Simonin, L., Masquelier, C., & Croguennec, L. (2018). High rate performance for carbon-coated $Na_3V_2(PO_4)_2F_3$ in Na-ion batteries. *Small Methods*. https://doi.org/10.1002/smtd.201800215

Chen, L., Feng, W., Pu, Z., Wang, X., Su, W., Li, M., Song, C., Shi, Z., & Zheng, Y. (2019). Effects of citric acid on the preparation of a $LiFePO_4$@C cathode material assisted by biomineralization. *International Journal of Electrochemical Science, 14*, 8048–8057. https://doi.org/10.20964/2019.08.78

Dacek, S. T., Richards, W. D., Kitchaev, D. A., & Ceder, G. (2016). Structure and dynamics of fluorophosphate Na-ion battery cathodes. *Chemistry of Materials, 28*(15), 5450–5460. https://doi.org/10.1021/acs.chemmater.6b01989

Gaddam, R. R., Katzenmeier, L., Lamprecht, X., & Bandarenka, A. S. (2021). Review on physical impedance models in modern battery research. *Physical Chemistry Chemical Physics, 23*(23), 12926–12944. https://doi.org/10.1039/D1CP00673H

Guo, J.-Z., Gu, Z.-Y., Du, M., Zhao, X.-X., Wang, X.-T., & Wu, X.-L. (2023). Emerging characterization techniques for delving polyanion-type cathode materials of sodium-ion batteries. *Materials Today*. https://doi.org/10.1016/j.mattod.2023.03.020

Harper, G., Sommerville, R., Kendrick, E., Driscoll, L., Slater, P., Stolkin, R., Walton, A., Christensen, P., Heidrich, O., Lambert, S., Abbott, A., Ryder, K., Gaines, L., & Anderson, P. (2019). Recycling lithium-ion batteries from electric vehicles. *Nature, 575*(7781), 75–86. https://doi.org/10.1038/s41586-019-1682-5

Hu, Y., Wu, L., Liao, G., Yang, Y., Ye, F., Chen, J., Zhu, X., & Zhong, S. (2018). Electrospinning synthesis of Na_2MnPO_4F/C nanofibers as a high voltage cathode material for Na-ion batteries. *Ceramics International, 44*(15), 17577–17584. https://doi.org/10.1016/j.ceramint.2018.06.236

Huang, H.-B., Liu, C.-L., Yang, Y., & Luo, S. (2022). Citric acid-assisted synthesis of $Na_3V_2(PO_4)_3$/C composite as high-performance electrode material for sodium-ion batteries. *Ionics, 28*(10), 4631–4639. https://doi.org/10.1007/s11581-022-04696-z

Jin, T., Li, H., Zhu, K., Wang, P.-F., Liu, P., & Jiao, L. (2020). Polyanion-type cathode materials for sodium-ion batteries. *Chemical Society Reviews, 49*(8), 2342–2377. https://doi.org/10.1039/C9CS00846B

Kim, S.-W., Seo, D.-H., Kim, H., Park, K.-Y., & Kang, K. (2012). A comparative study on Na_2MnPO_4F and Li_2MnPO_4F for rechargeable battery cathodes. *Physical Chemistry Chemical Physics, 14*(10), 3299–3303. https://doi.org/10.1039/C2CP40082K

Kim, T., Choi, W., Shin, H.-C., Choi, J.-Y., Kim, J. M., Park, M.-S., & Yoon, W.-S. (2020). Applications of voltammetry in lithium ion battery research. *Journal of Electrochemical Science and Technology, 11*(1), 14–25. https://doi.org/10.33961/jecst.2019.00619

Langford, J. I., & Wilson, A. J. C. (1978). Scherrer after sixty years: A survey and some new results in the determination of crystallite size. *Journal of Applied Crystallography, 11*(2), 102–113. https://doi.org/10.1107/S0021889878012844

Lin, X., et al. "Exploiting Na_2MnPO_4F as a High-Capacity and Well-Reversible Cathode Material for Na-Ion Batteries." *RSC Advances* 4, no. 77 (2014): 40985–40993. https://doi.org/10.1039/C4RA05336B.

Ling, R., Cai, S., Shen, K., Sang, Z., Xie, D., Sun, J., Xiong, K., Guo, J., & Sun, X. (2019). Dual carbon-confined Na_2MnPO_4F nanoparticles as a superior cathode for rechargeable sodium-ion battery. *Ceramics International*. https://doi.org/10.1016/j.ceramint.2019.06.235

Niu, Y., Zhao, Y., & Xu, M. (2023). Manganese-based polyanionic cathodes for sodium-ion batteries. *Carbon Neutralization, 2*(2), 150–168. https://doi.org/10.1002/cnl2.48

Patterson, A. L. (1939). The Scherrer formula for X-ray particle size determination. *Physical Review, 56*(10), 978–982. https://doi.org/10.1103/PhysRev.56.978

Rojo, T., Forsyth, M., Lee, H. S., Zhang, W., & Armand, M. (2018). Sodium-ion batteries. *Advanced Energy Materials, 8*(17), 1800880. https://doi.org/10.1002/aenm.201800880

Safitri, M., Zainuri, M., Subhan, A., Putri, S. S. H., & Putri, F. L. V. P. (2023). The influence of variations carbon content on the structure of Na_2MnPO_4F/C cathode material. *Journal of Physics: Conference Series, 2498*, 012029. https://doi.org/10.1088/1742-6596/2498/1/012029

Siburian, R., Raja, S. L., Supeno, M., & Simanjuntak, C. (2019). Application of coconut battery waste to graphic as an alternative electrode on primary battery cells. *Abdimas Talenta: Jurnal Pengabdian Kepada Masyarakat, 4*(2), 668–673. https://doi.org/10.32734/abdimastalenta.v4i2.4202

Sui, Y., Shi, Z., Hu, Y., Zhang, X., Wu, X., & Wu, L. (2021). A pre-oxidation strategy to improve architecture stability and electrochemical performance of Na_2MnPO_4F particles-embedded carbon nanofibers. *Journal of Colloid and Interface Science*. https://doi.org/10.1016/j.jcis.2021.06.081

Sun, Y., Shi, X.-L., Yang, Y.-L., Suo, G., Zhang, L., Lu, S., & Chen, Z.-G. (2022). Biomass-derived carbon for high-performance batteries: From structure to properties. *Advanced Functional Materials*. https://doi.org/10.1002/adfm.202201584

Wu, L., Hu, Y., Zhang, X., Liu, J., Zhu, X., & Zhong, S. (2018). Synthesis of carbon-coated Na_2MnPO_4F hollow spheres as a potential cathode material for Na-ion batteries. *Journal of Power Sources, 374*, 40–47. https://doi.org/10.1016/j.jpowsour.2017.11.029

Wu, X., Zheng, J., Gong, Z., & Yang, Y. (2011). Sol–gel synthesis and electrochemical properties of fluorophosphates $Na_2Fe_1-xMn_xPO_4F/C$ (x = 0, 0.1, 0.3, 0.7, 1) composite as cathode materials for lithium ion battery. *Journal of Materials Chemistry, 21*, 18630–18637. https://doi.org/10.1039/C1JM13578C

Yao, Q., Zheng, C., Liu, K., Wang, M., Song, J., Cui, L., Dou, S. X., Bai, Z., & Yang, J. (2024). Bi nanospheres embedded in N-doped carbon nanowires facilitate ultrafast and ultrastable sodium storage. *Advanced Science, 11*(28), e2401730. https://doi.org/10.1002/advs.202401730

Zhang, J. (2017). *Development of property prediction methods for sodium-ion battery electrolytes*. Queen's University Belfast Research Portal. https://pure.qub.ac.uk/en/studentTheses/development-of-property-prediction-methods-for-sodium-ion-battery

Zhang, L., Dai, Y., Li, C., Dang, Y., Zheng, R., Wang, Z., Wang, Y., Cui, Y., Arandiyan, H., Shao, Z., Sun, H., Zhuang, Q., & Liu, Y. (2024). Recent advances in electrochemical impedance spectroscopy for solid-state batteries. *Energy Storage Materials*. https://doi.org/10.1016/j.ensm.2024.103378

Zhang, S., Gong, G., Wang, H., Chen, S., Wang, J., & Qi, J. (2025). Advances and challenges of the spray drying technology: Towards accurately constructing inorganic multi-functional materials and related applications. *Sustainable Materials and Technologies*. https://doi.org/10.1016/j.susmat.2025.e01250

Zheng, Y., Zhang, P., Wu, S. Q., Wen, Y. H., Zhu, Z. Z., & Yang, Y. (2013). First-principles investigations on the Na_2MnPO_4F as a cathode material for Na-ion batteries. *Journal of The Electrochemical Society, 160*(6), A927–A932. https://doi.org/10.1149/2.127306jes

Zhong, Y., Wu, Z., Tang, Y., Xiang, W., Guo, X., & Zhong, B. (2015). Micro-nano structure Na_2MnPO_4F/C as cathode material with excellent sodium storage properties. *Materials Letters*. https://doi.org/10.1016/j.matlet.2015.01.110

Zhu, X., Li, Q., Fang, Y., Liu, X., Xiao, L., Ai, X., Yang, H., & Cao, Y. (2016). Graphene-modified TiO_2 microspheres synthesized by a facile spray-drying route for enhanced sodium-ion storage. *Particle & Particle Systems Characterization, 33*(11), 1–8. https://doi.org/10.1002/ppsc.201500216

Biography of Author

Nugraha Ramadhan, S.Si., obtained his Bachelor's degree in Physics from the Department of Physics, Faculty of Science and Data Analytics, Institut Teknologi Sepuluh Nopember (ITS), Indonesia. His research focuses on material physics, particularly nanomaterials, photocatalysis, and sustainable innovation. His academic experiences include participation in scientific competitions, research projects, and professional engagements such as an internship at Tiket.com, laboratory assistantship, and freelance teaching. His expertise focuses on material physics and its applications in environmental and industrial fields.

- Email: nugrahamdhan@gmail.com
- ORCID: N/A
- Web of Science ResearcherID: N/A
- Scopus Author ID: N/A
- Homepage: N/A